Experimental Validation of Indirect Liquid Cooling Computational Thermal Modeling

by

Isabel K. Alvarez

Submitted to the Department of Mechanical Engineering in partial fulfillment of the requirements for the degree of

BACHELOR OF SCIENCE IN MECHANICAL AND OCEAN ENGINEERING

at the

MASSACHUSETTS INSTITUTE OF TECHNOLOGY

May 2024

© 2024 Isabel K. Alvarez. All rights reserved.

The author hereby grants to MIT a nonexclusive, worldwide, irrevocable, royalty-free license to exercise any and all rights under copyright, including to reproduce, preserve, distribute and publicly display copies of the thesis, or release the thesis under an open-access license.

Authored by: Isabel K. Alvarez

Department of Mechanical Engineering

May 10, 2024

Certified by: Julie Chalfant

Research Scientist, Thesis Supervisor

Certified by: Michael Triantafyllou

Professor of Mechanical and Ocean Engineering, Thesis Supervisor

Accepted by: Kenneth Kamrin

Professor of Mechanical Engineering

Undergraduate Officer, Department of Mechanical Engineering

Experimental Validation of Indirect Liquid Cooling Computational Thermal Modeling

by

Isabel K. Alvarez

Submitted to the Department of Mechanical Engineering on May 10, 2024 in partial fulfillment of the requirements for the degree of

BACHELOR OF SCIENCE IN MECHANICAL AND OCEAN ENGINEERING

ABSTRACT

Indirect dry-interface liquid cooling for electronics offers a modular and lightweight approach to thermal management. As part of development for the Navy's integrated Power and Energy Corridor (NiPEC), multiple computational thermal analyses of this cooling method have been conducted but not yet tested against experimental results. NiPEC involves the deployment of converter units referred to as integrated Power Electronics Building Blocks (iPEBBs), which experience heat generation from four rows of MOSFET switches and a transformer. The goal of thermal simulations is to predict the liquid flow rate through a cold plate given a heat flux which will keep the iPEBBs below 100°C. Experimental data on indirect liquid cooling of a layered substrate was collected with varied power, temperatures and flow rates. The data was verified through a STAR-CCM+ CFD simulation by David Hernandez, then used as a training and test set for a physics-informed neural network (PINN) model by Aniruddha Bora. The PINNs simulations were shown to improve in consistency and accuracy when trained on data gathered in the experimental trials. The collected experimental data set is available to the public for training and testing computational models.

Thesis supervisor: Julie Chalfant

Title: Research Scientist

Thesis supervisor: Michael Triantafyllou

Title: Professor of Mechanical and Ocean Engineering

Acknowledgments

I would like expresses my gratitude to Dr. Chalfant and Prof. Triantafyllou for their guidance and supervision of this thesis. I greatly appreciate the invaluable insights that Prof. Emeritus Chryssotomidis and Prof. Triantafyllou offered as my undergraduate advisors. I would also like to thank Dr. Bora for his collaboration, as well as David Hernandez for designing and running CFD simulations. MATLAB scripts and sensors provided by the 2.671 staff were instrumental in this thesis. Lastly, I would like to thank my mother and father for their love and support, and for always encouraging my curiosity.

This material is based upon research supported by the U.S. Office of Naval Research (ONR) under award number ONR N00014-21-1-2124 Electric Ship Research and Development Consortium; and by the National Oceanic and Atmospheric Administration (NOAA) under Grant Number NA22OAR4170126-MIT Sea Grant College Program.

Contents

Ti	itle page	1
Al	bstract	3
A	cknowledgments	5
Li	st of Figures	9
Li	st of Tables	13
1	Introduction 1.1 Thesis Objective	15 16
2	Background 2.1 Indirect Liquid Cooling of iPEBBs 2.2 Modeling 2.2.1 Adiabatic Theory 2.2.2 CFD Simulation 2.2.3 PINNs	19 19 19 19 21 21
3	Experimental Design 3.1 Experimental Rig	23 23 23 25 26
4	Results and Discussion4.1 Repeatability of Experiment	29 29 33 36
5	Conclusions and Future Work	41
Re	eferences	43
\mathbf{A}	Material Properties	47

List of Figures

1	Schematic showing proposed segment of the power electronics arrangement	
	within a ship hull, modified from [7]. iPEBBs are stacked in a server rack	4.0
2	configuration.	16
2	iPEBB design showing location of Silicon Carbide (SiC) MOSFETs and high	
	frequency transformer, from [8]. The MOSFET bridges are the main source	
	of thermal energy within the iPEBB	17
3	Diagram showing simplified thermal resistor network of the experiment. By	
	neglecting heat exchange with the environment, heat flow Q_{in} is equated to	
	Q_{out} of the system to relate the flow rate and the temperature drop between	
	the inlet and outlet of the cold plate liquid	20
4	Experimental rig with four power resistors (shown in orange) adhered to a	
	layered substrate which is in thermal contact with a cold plate	23
5	Graphic showing placement of temperature sensors from an exploded side	
	view and top view on the experimental rig. Additional details on temperature	
	sensors labeled (a) through (h) are given in Table 1. Sensors (c), (d), and	
	(e) were placed 40 mm in from the edge of the aluminum plates. Additional	2.4
0	material information is given in Appendix A	24
6	Graphic showing temperature sensor electronic architecture for connecting	
	three different types of sensors to an Arduino Leonardo for data collection.	
	Temperature sensor range and accuracy is given in Table 2. The Analog De-	
	vices DS18B20 digital temperature sensors were used in a Sparkfun waterproof	25
7	housing.	25
7	Graphic showing the experimental set up. The power resistors shown in orange	
	on the experimental stack were heated by two Extech Adjustable Switching Mode Power Supplies. Water was circulated through the cold plate in the stack	
	and the IKA RC 2 Basic Chiller-Circulator with controllable inlet temperature	
	and flow rate. The heat flows in and out of the system are labeled as Q_{in} and	
	Q_{out}	26
8	CFD simulation courtesy of David Hernandez with a heat flow in of 200W,	20
O	inlet temperature of 15°C, and flow rate of 2.34 L/min. This image is from	
	one of nine runs compared to experimental data and PINNs simulation results.	
	The results from all nine CFD runs are given in Appendix B	27
	The results from all time of b ratio are given in rippoint b	

9	Graph real time sensor readings across a ten minute trial with the experimental conditions of 260W, 15°C inlet temperature, and 2.4 L/min flow rate. As	
	stated in Table 2, the K-type thermocouples have the largest error which is	
	visible in the sensor noise of those four probes: ambient, resistor, face, and	
	side. Discrete steps in temperature are observed due to behavior of the K-type	
	thermocouple amplifier [25]	30
10	Graphs comparing measured system temperatures for three repeated trials	50
10	at (a) heat flow Q_{in} of 150W; (b) heat flow Q_{in} of 260W. The inlet tem-	
	perature is prescribed at 15°C, and is consistent across all nine trials. The	
	other three temperatures are observed to decrease with slower liquid cooling	
	flow rate and lower power across all trials. The highest variation in trials	
	is observed on the face, which is measured with the high-uncertainty K-type	
	thermocouple. As the other three locations have significantly less difference	
	between trials and were measured with more accurate temperature sensors,	
	the thermocouple sensor error largely accounts for observed face temperature	
	variation. Plotted data points for repeated trials with lower variation are	
	visibly near-indistinguishable	31
11	Graphs comparing the predicted values by PINNs, normalized by experimen-	01
	tal values for (a) flow rate; (b) middle stack temperature. Error bars represent	
	95% confidence intervals, calculated with error propagation for experimental	
	and simulation results. The expected flow rate is included in all PINNs simu-	
	lations trained on experimental data but only included in two for simulations	
	not trained on data. One trial included the expected middle stack tempera-	
	ture for both models with and without training data, but accuracy increased	
	for the simulations given data	34
12	Three cross sections from thermal simulations: (top) Simcenter STAR-CCM+	
	CFD for 200W 15°C 2.34 L/min, courtesy of David Hernandez; (middle)	
	PINNs without data for 260W 20° C 2.34 L/min; (bottom) PINNs with exper-	
	imental data for 260W 20 $^{\circ}$ C 2.34 L/min. Though the absolute temperatures	
	are expected to differ, the distributions are expected to remain similar. The	
	PINNs simulation not given experimental data has a more similar thermal pro-	
	file to CFD than the PINNs simulation trained on experimental data. Note	
	the differing colormap scales of the three temperature distributions	35
13	Graph of calculated heat flow out against measured heat flow into the system	
	for experimental results, CFD, and PINNs. A line is drawn for $Q_{out} = Q_{in}$,	
	the adiabatic condition. All three data sets follow the theory as expected, but	
	larger variation is seen in the PINNs data. A significant outlier is seen in the	
	PINNs simulation, which is inherently a stochastic process and will sometimes	
	settle on a non-optimal solution, highlighting the necessity of multiple trials.	37

14	Comparison of the temperature drop across the face and middle of the stack:	
	(a) by heat flow rate; (b) by inlet velocity. Experimental results, CFD, and	
	PINNs simulations all follow a similar upward trend by heat flow rate, but not	
	for inlet velocity. Discrepancies between experimental and simulated results is	
	partially due to sensor error and uncertainty in material thermal properties.	
	Specifically, PGS thermal conductivity is pressure dependent and was only	
	recently characterized at lower pressures [10]	38
15	Bar graph showing the experimental measurement as well as CFD and PINNs	
	predictions for temperature at four points on the stack: (d) In ₁ , (e) In ₂ ,	
	(f) Edge, and (c) Face, as labeled in Fig. 5. The experimental conditions	
	were 15°C inlet temperature, 150 W, and 1.4 L/min flow rate. The PINNs	
	model was trained on the experimental edge and face temperature, so it is	
	expected that the experimental value is included in the 95% confidence interval	
	for PINNs. In three cases, the PINNs model predicted values closer to the	
	experimental set up than the CFD model. This is not surprising as the thermal	
	resistance of each material in the experimental rig is not known precisely,	
	though both models were given the same initial estimates	39

List of Tables

	Type and Location of Thermal Sensors shown in Fig. 5	
	Geometry and Properties of Materials in the Experimental Rig	
4	CFD Simulation Results	49

1 Introduction

The electrification of marine vessels has been an attractive idea for decades from both environmental and tactical perspectives, yet its actual implementation has only recently begun. With concerns over climate change and pollution escalating, the International Maritime Organization (IMO) committed in 2018 to decarbonizing shipping, pursuing a 70% greenhouse gas emission reduction by 2050 [1].

Five years later, the IMO accelerated their timeline, striving to reach net-zero greenhouse gas emissions close to 2050 [2]. The United States Navy made their intentions of moving toward electrification clear in the 2019 Naval Power and Energy System Technology Development Roadmap (NPES) [3]. The report states "electricity allows moving large amounts of energy from one place to another, controllably and quickly, making the energy resource (power generated by prime movers) extremely fungible" [3]. Silent running, increased maneuverability, support of high-power modules, and reduction of emissions through electrification are desirable qualities across industrial and marine applications.

Energy storage and management was long pointed to as the barrier to electrification of commercial shipping, but more updated studies have demonstrated challenges are shifting towards operational instead of technological [4], [5]. However, Naval applications of electrification still require further technological development. In 2022, a five year program was proposed by the Office of Naval Research (ONR) to develop the Power Electronic Power Distribution System (PEPDS) [6]. Figure 1 shows a ship hull section with one proposed NiPEC layout.

To meet Navy system requirements, research is being conducted around the Navy integrated Power Electronics Building Block (iPEBB), Navy integrated Power and Energy Corridor (NiPEC), control, and simulation. iPEBBs are the modular, lightweight, self-contained base unit for electrical distribution that NiPEC utilizes to build out safe and resilient high-power shipboard energy systems, shown in Fig. 2. The PEPDS program is looking to culminate in a megawatt-level test bed, which requires additional research into thermal management of iPEBBs while maintaining the modular and lightweight specifications.

The traditional methods of thermal management, direct liquid cooling and finned airto-air heat exchangers, violate the design constraints of an iPEBB. Liquid connections to the iPEBBs are prohibited, and the units must be robust, compact, and under 35 lbs [6]. One iPEBB must be able to dissipate 9.6kW of heat generated in the transistor system and 1.2kW of heat generated by the high frequency transformer while staying under 100°C [7], [9]. The location of the heat-generating components are highlighted in Fig. 2. Recent research has been conducted towards meeting these challenging requirements through indirect liquid

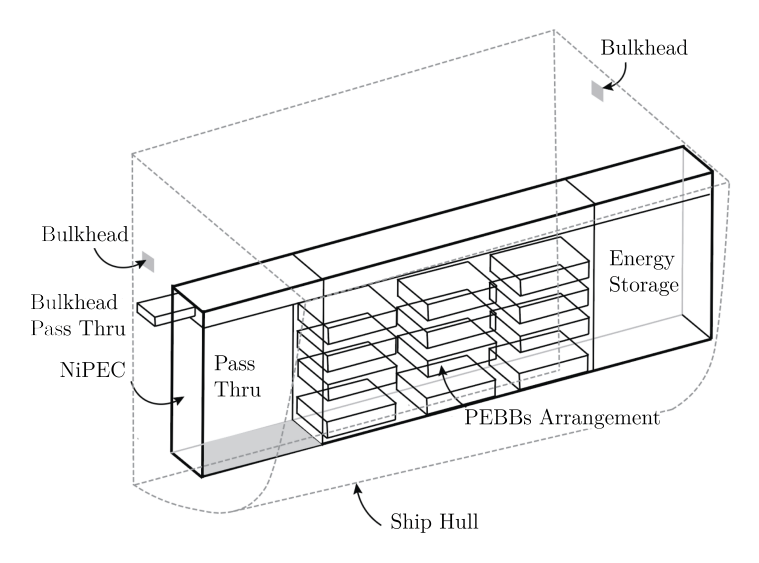


Figure 1: Schematic showing proposed segment of the power electronics arrangement within a ship hull, modified from [7]. iPEBBs are stacked in a server rack configuration.

cooling, including thermal modeling and simulation [9], [10]. Dry-interface liquid cooling uses a cold plate in contact with the iPEBB to remove heat, and relies on the low contact resistance between the cold plate and the iPEBB provided by thermal interface materials. Computational fluid dynamic (CFD) modeling of the indirect liquid cooling solution yielded promising results, but has not been experimentally validated.

The PEPDS initiative also looks to further simulation capabilities. Physics-informed neural networks (PINNs) could offer a faster and more powerful simulation with predictive powers for unconventional thermal management systems such as indirect liquid cooling [11]. Experimental data must be collected to validate this emerging computational tool.

1.1 Thesis Objective

There are still many unknown elements within the NiPEC design, including the behavior of developmental electronic components inside the iPEBB. Until the testbed design is finalized, the ability to quickly and effectively iterate on the cooling system is critical. CFD and PINNs are both powerful tools for informing the dry-interface cooling system parameters based on the most current requirements of the iPEBB. Experimental data verifying CFD for an analogous system will improve confidence of simulation results. PINNs have the potential to provide accurate simulation results at higher speeds if the training and test data encompass the range of expected cooling conditions in the system. Neither experimental data sets have been previously collected for dry interface liquid cooling of a layered substrate based on the most recent iPEBB design.

Thermal experiments on dry-interface liquid cooling were conducted to validate a computational fluid dynamic model built in STAR-CCM+ and a physics-informed neural network (PINN) assessment. The experimental data serve as a training and testing set for the PINNs model, and were used to assess the CFD model. Inlet temperature, flow rate, and power were

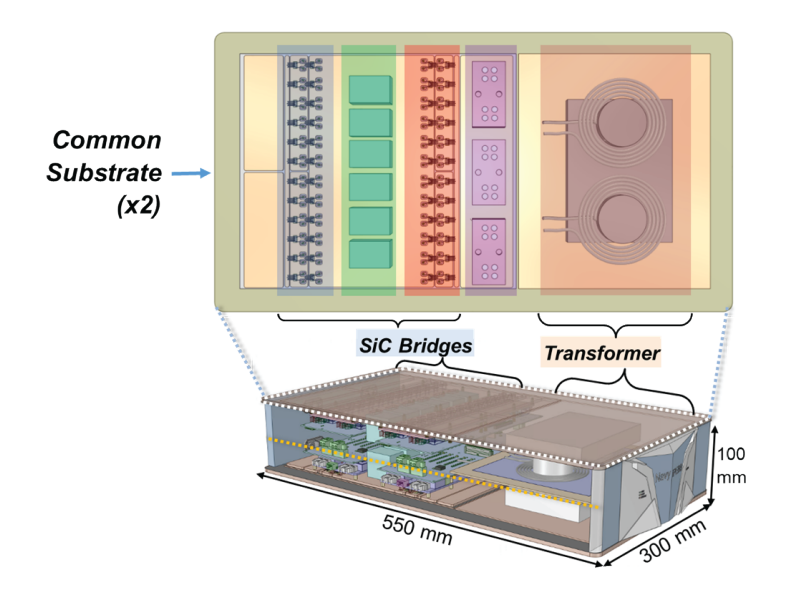


Figure 2: iPEBB design showing location of Silicon Carbide (SiC) MOSFETs and high frequency transformer, from [8]. The MOSFET bridges are the main source of thermal energy within the iPEBB.

varied with steady-state system temperatures recorded. Results from this analysis were used to comment on the predictive power of PINNs modeling and validity of physical assumptions behind the simulations. As specifications for the iPEBBs evolve, improved and verified modeling will allow for more effective design iteration. PINNs simulation and physics-informed deep operator networks (DeepONets) also have applications to a wider variety of thermal management systems once further developed.

2 Background

2.1 Indirect Liquid Cooling of iPEBBs

The Navy iPEBB relies on Silicon-Carbide (SiC) power transistors to support high loads and faster switching than current silicon-based technologies and a high frequency transformer to electrically isolate the distribution side from the load side of the iPEBB [6]. The SiC MOSFET bridges are expected to collectively generate 9.6 kW of heat through conduction and switching losses. The high frequency transformer is expected to generate up to 1.2 kW of heat, and provides the 100°C operational constraint [7]. The total heat flux that must be removed from the iPEBB is 3.3 W/cm² across the top and bottom surfaces.

The iPEBB base units are anticipated to be vertically stacked to build out a configurable shipboard power system. The indirect liquid cooling system must be fully integrated into the stack and still allow for quick replacement of each individual unit. Indirect liquid cooling is uncommon in these applications because contact resistance between the heat source and cooling mechanism drastically decreases efficiency. Thermal interfaces are being explored to reduce this inefficiency, but it still presents a significant challenge.

Within that stack, the current design for indirect liquid cooling is to have a thermal interface between the concentrated heat loads of each iPEBB and the cooling plate. Pyrolytic Graphite Sheets (PGS) under low pressure (below 10 psi) were explored as potential thermal interface material for this specific application [10]. A mechanical load must be maintained between the iPEBB surface and the cold plate to lower the thermal resistance of the PGS, and the mechanism and cold plate must be incorporated into the modular stack. The mechanical load must also have a quick-release mechanism for the removal and replacement of iPEBBs [12]. This unique configuration currently relies on simulation to predict cooling behavior.

2.2 Modeling

2.2.1 Adiabatic Theory

The simplest thermal model for the indirect liquid cooling is the adiabatic model which equates the heat flow in from the source to heat flow removed by the cooling system. The thermal network being examined is shown in Fig. 3. Note that convection to air is approximated as having significantly larger thermal resistance than conduction and therefore left out of the thermal network.

This model will underestimate the velocity or the temperature difference as it neglects

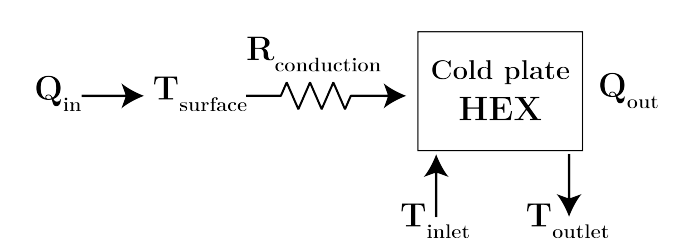


Figure 3: Diagram showing simplified thermal resistor network of the experiment. By neglecting heat exchange with the environment, heat flow Q_{in} is equated to Q_{out} of the system to relate the flow rate and the temperature drop between the inlet and outlet of the cold plate liquid.

heat flux from the ambient environment. It also neglects any heat added due to viscous effects in the liquid cooling loop.

The rate of heat flow out of the system, Q_{out} , is calculated as:

$$Q_{out} = \dot{m}c_p \Delta T = \rho A v c_p \Delta T \tag{1}$$

where ρ represents density of water, A is the interior cross-sectional area of the pipe, v is water velocity, c_p is the specific heat capacity of water under constant pressure, and ΔT is the temperature difference between the inlet and outlet.

The inlet to outlet temperature drop, ΔT can be related to velocity or mass flow rate, \dot{m} , under adiabatic conditions as:

$$\Delta T = \frac{Q_{in}}{\dot{m}c_p} = \frac{Q_{in}}{\rho Av \, c_p} \tag{2}$$

The thermal resistance from the surface of the stack to the cold plate is estimated as a summation of the conductive resistances across each layer, calculated as:

$$R_{conduction} = \frac{L}{kA} \tag{3}$$

where L is length in the path parallel to heat flux, k is thermal conductivity, and A is the cross-sectional area perpendicular to heat flow.

The thermal resistance from the bulk of the cold plate to the steel tubing is estimated as:

$$R_{conduction,cyl} = \frac{ln(r_2/r_1)}{2\pi Lk} \tag{4}$$

where r_2 and r_1 are outer and inner radius of the cylindrical shell respectively, and L is the length of the shell. Both conductive resistance relationships are derived from Fourier's law for heat conduction.

Several simplifying assumptions were employed, including adiabatic boundaries and uniform in-plane temperature were used to quickly estimate the temperature profile. This rough estimate provides basic intuition for how the experimental set up was expected to behave, and adds confidence to the evaluation of simulation results.

2.2.2 CFD Simulation

Simcenter STAR-CCM+ is commercial computational fluid dynamics simulation software which utilizes finite element analysis (FEA) to model complex systems. The system is physically discretized into a mesh, and within each finite element, governing differential equations are numerically solved. FEA is generally accepted as the standard for the computation thermal analysis.

CFD has been applied previously to indirect liquid cooling design. Experimental validation of CFD modeling for indirect liquid cooling of electronics has also been carried out. Cheng et al. in 2006 found that CFD simulation results were within 2% of the measurement results for indirect liquid cooling of a compact multichip module with a thermal grease interface [13]. Though the experimental conditions differ from the iPEBBs cooling experimental design, the physics being simulated have significant overlap. The Liu et al. study successfully combined data-driven FEA, validated by experimentation, with a Gaussian process-based (GP) surrogate model to rapidly converge on an optimal cooling plate geometry for batteries [14]. The physics-based simulation was found to be 90% faster than the experimental method and accurately predicted the maximum battery temperature. CFD is expected to produce highly accurate results with low uncertainty, and is therefore used to validate the data set and as a standard against PINNs.

2.2.3 PINNs

Physics-Informed Neural Networks (PINNs) operate at the intersection of physics-based modeling and machine learning, offering promising solutions for a wide range of scientific and engineering problems. PINNs leverage neural networks to learn complex relationships within data while incorporating fundamental physical principles into the learning process. PINNs are emerging as a tool to simulate complex physical systems, including fluid dynamics, solid mechanics, and electromagnetics, due to their ability to efficiently solve nonlinear partial differential equations (PDEs). However, as the solution is based on optimization, the models tend to require careful tuning and can be sensitive to the initial conditions and hyperparameters. PINNs can settle on local solutions instead of globally optimal solutions, leading to outliers. Modifications have been developed by researchers to make PINNs simulations more robust to these sensitivities [15]–[18]. Furthermore, PINNs are configured to solve specific partial differential equations based on a set of parameters, which means that any alteration in the design parameters necessitates retraining the network to accommodate the new conditions. To circumvent such issues and to tackle with the family of solutions for different parameters, Lu et al. came up with the idea of a deep operator network (DeepONet) that allows to maps between two functional spaces [19], [20].

The development of PINNs has been motivated by the limitations of traditional computational methods in capturing complex systems physics and handling noisy or sparse data. Traditional numerical methods typically use grid-based discretization and iterative solving processes, which can become computationally intensive as the dimensionality rises or when dealing with problems that span multiple scales. In contrast, PINNs offer a data-driven model that learns directly from observations, removing the need for mesh generation and iterative solving. By incorporating physical principles as constraints during training, PINNs

can effectively regularize the learning process, leading to more accurate predictions and improved generalization capabilities even when given small data sets. These qualities make PINNs especially powerful for analyzing complex thermodynamic systems, and have been found to even be effective with unknown boundary conditions [21], [22]. PINNs simulations have not yet been applied to indirect dry-interface liquid cooling systems, so learning and test data sets are required to train the model. This thesis provides the experimental training and test data for use in development of PINNs models of power electronics dry-interface liquid cooling.

3 Experimental Design

3.1 Experimental Rig

As iPEBBs are still in development, a modified version of the pressure proximity rig designed and built by Joushua Padilla in his 2023 Master's thesis was used as the basis of experimentation [10]. The pressure proximity rig shown in Fig. 4 consists of a cold plate, two aluminum plates, PGS as thermal interfaces, and four power resistors to deliver heat.

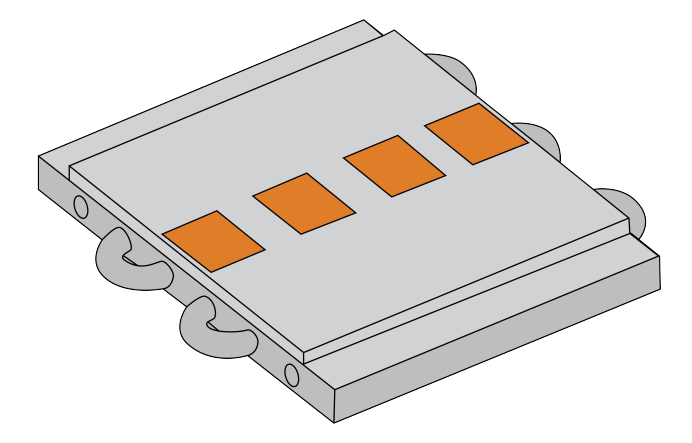


Figure 4: Experimental rig with four power resistors (shown in orange) adhered to a layered substrate which is in thermal contact with a cold plate.

Threaded fasteners are used to create pressure between the layered substrate, the cold plate, and the power resistors to reduce the thermal resistance of PGS to a known value based on the pounds per square inch of the system. Temperature sensors are placed at five points on the physical rig, labeled in the side view of Fig. 5. Two holes were milled 40 mm into the side of the middle aluminum plate to measure the internal temperature of the stack. Three more temperature sensors were included to measure the ambient temperature, and the inlet and outlet temperature of the water flowing through the cold plate.

3.2 Sensors and Data Collection

Temperature data from the three different types of thermal sensors was collected through an Arduino Leonardo as shown in Fig 6, and the serial output for each trial was logged with PuTTY. The data was then analyzed in MATLAB. While using the same type of thermal

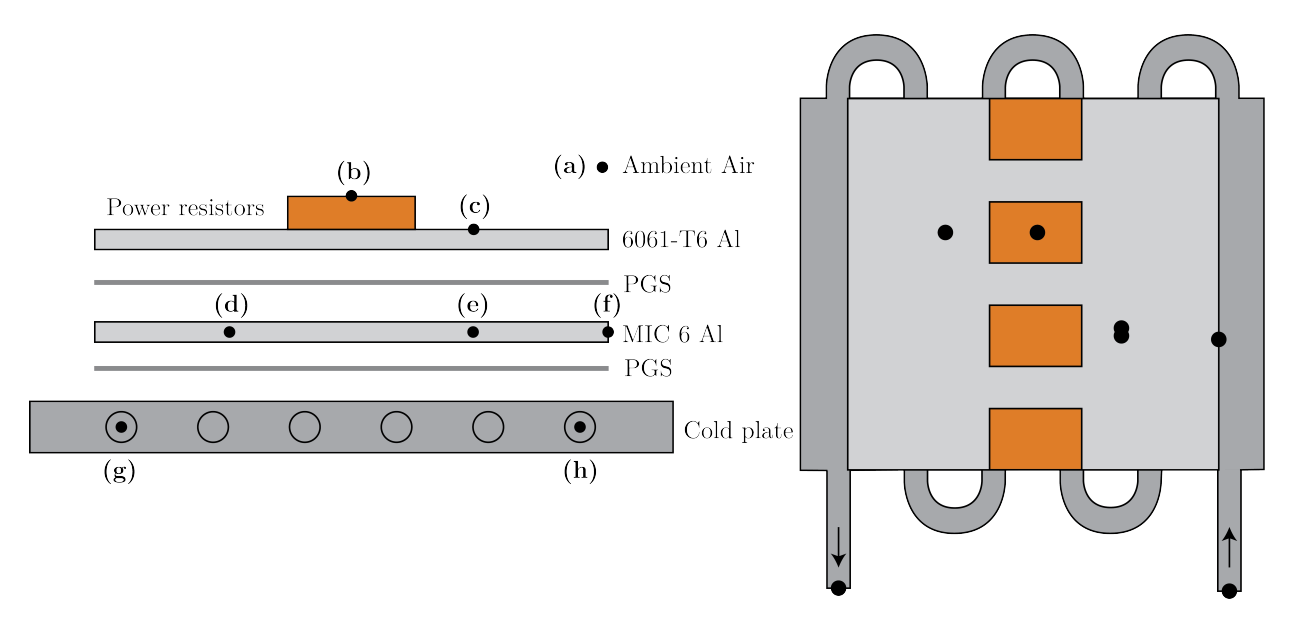


Figure 5: Graphic showing placement of temperature sensors from an exploded side view and top view on the experimental rig. Additional details on temperature sensors labeled (a) through (h) are given in Table 1. Sensors (c), (d), and (e) were placed 40 mm in from the edge of the aluminum plates. Additional material information is given in Appendix A.

sensor throughout the system would have been ideal, different environmental and spatial constraints lead to the selection of the three sensor types. Additional boards were required to connect the Adafruit thermocouples and the Vernier surface thermistors.

Information for all five types of sensors is compiled in Table 2. The digital temperature sensors made by Analog Devices were sealed in a Sparkfun waterproof housing. All experimental measurements were conducted in the 0°C to 55°C range and the Vernier sensors were not subjected temperatures higher than 40°C, so the reported uncertainty is applicable. The three different temperatures vary most critically in uncertainty. Both the pressure and flow rate sensors were reported to have large uncertainty, but lengths were taken to reduce this uncertainty. The flow rate sensor was calibrated by measuring water volume over a known period of time across five different flow rates. Increments of known weight were used to

Table 1: Type and Location of Thermal Sensors shown in Fig. 5

Sensor Name		Type			
(a)	Ambient	K-type Thermocouple			
(b)	Resistor	K-type Thermocouple			
(c)	Face	K-type Thermocouple			
(d)	${ m In}_1$	Surface Thermistor			
(e)	${\rm In}_2$	Surface Thermistor			
(f)	Edge	K-type Thermocouple			
(g)	Outlet	Digital Temperature Sensor			
(h)	Inlet	Digital Temperature Sensor			

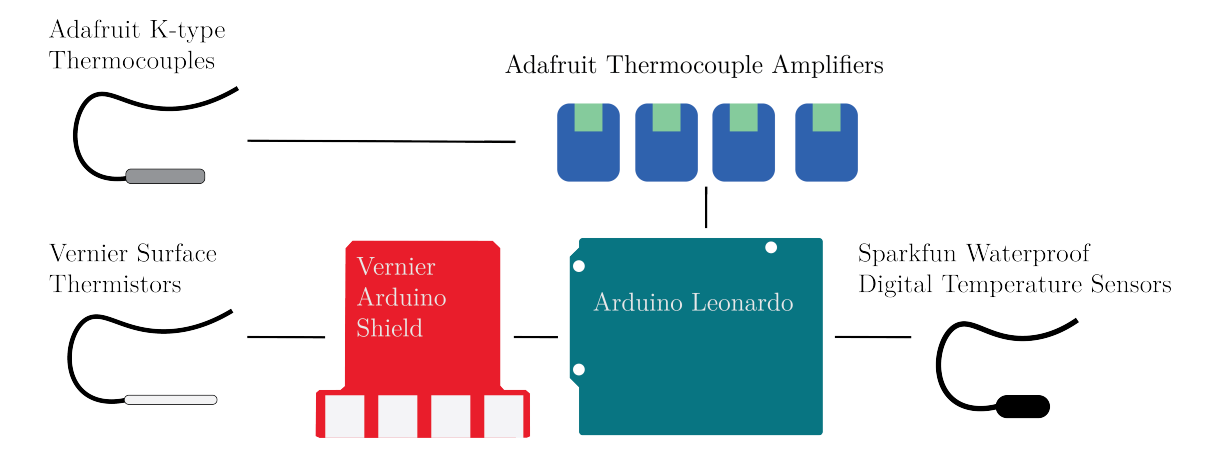


Figure 6: Graphic showing temperature sensor electronic architecture for connecting three different types of sensors to an Arduino Leonardo for data collection. Temperature sensor range and accuracy is given in Table 2. The Analog Devices DS18B20 digital temperature sensors were used in a Sparkfun waterproof housing.

calibrate and re-zero the pressure sensor.

3.3 Experimental Trials

The physical experimental set up is shown below in Fig. 7. Q_{in} represents the heat flux delivered by the two power supplies to the power resistors in the experimental stack. Q_{out} represents the heat flux removed by the chiller-circulator from the experimental stack through the cold plate. Water was used as the liquid in the chiller-circulator cold plate loop.

Two Extech Adjustable Switching Mode Power Supplies were wired to two resistors each, providing up to 520 Watts to the experimental stack. The cold plate in the experimental stack was connected through tubing to an IKA RC 2 Basic Chiller-Circulator, which was used to control inlet temperature and flow rate. The Digiten flow sensor was placed in the outlet flow path to measure the volumetric flow rate of the system.

To verify experimental repeatability, ten minute trials were taken three times over the course of several days for the lowest and highest power of the data set at three different flow rates. Once repeatability was established, the experimental conditions were expanded to a

Table 2: Complete sensor list with uncertainty and range used in experimental trials

Measurement Units		Sensor	Range	Uncertainty
Pressure	psi	TekScan I-Scan 5151 Mat	0-150	3-9% [23]
Flow rate	L/\min	Digiten FL-408	1-30	$\pm 0.6 [24]$
Temperature	$^{\circ}\mathrm{C}$	Adafruit K-Type Thermocouple	-250-400	$\pm 2^{\circ} [25]$
Temperature	$^{\circ}\mathrm{C}$	Vernier Surface Thermistor	0-40	$\pm 0.03^{\circ} [26]$
Temperature	$^{\circ}\mathrm{C}$	Analog Devices DS18B20	-10-85	$\pm 0.5^{\circ} [27]$

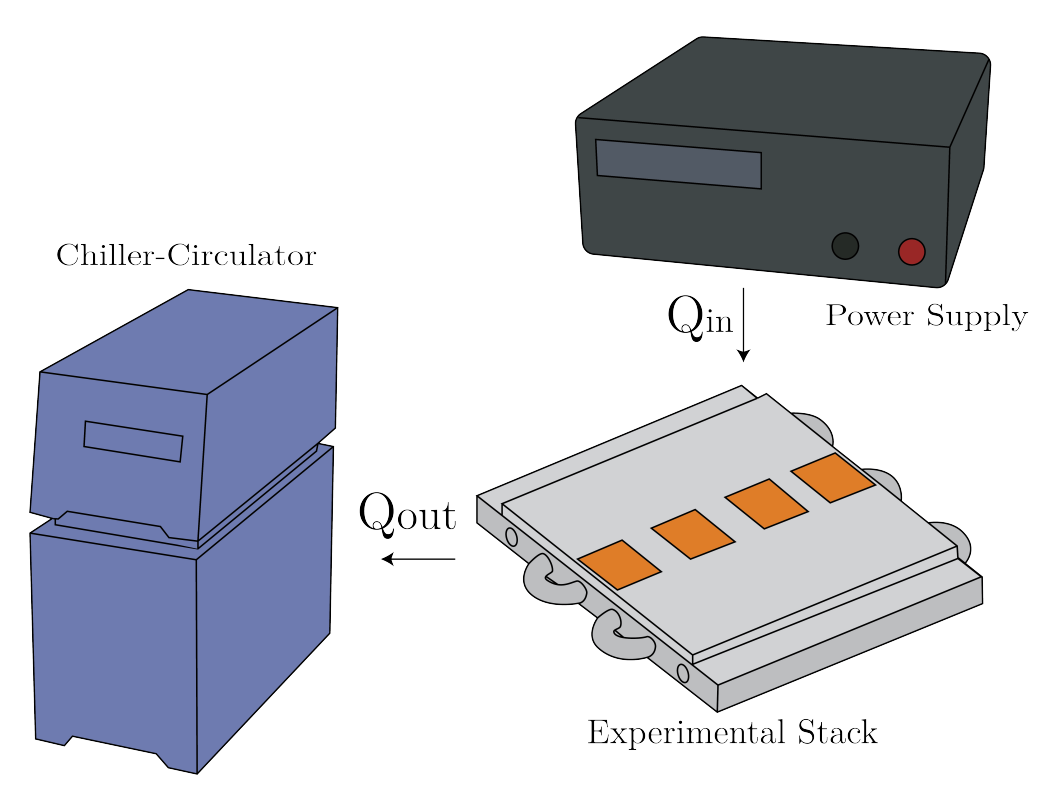


Figure 7: Graphic showing the experimental set up. The power resistors shown in orange on the experimental stack were heated by two Extech Adjustable Switching Mode Power Supplies. Water was circulated through the cold plate in the stack and the IKA RC 2 Basic Chiller-Circulator with controllable inlet temperature and flow rate. The heat flows in and out of the system are labeled as Q_{in} and Q_{out} .

total of four different powers, five different flow rates, and three inlet temperatures. The wide variety of experimental conditions were selected to provide a robust training and test data set for the PINNs model.

3.4 Simulation of Experimental Rig

Two different thermal simulation methods of the experimental rig were employed: CFD and PINNs. These simulations had differing constructions, boundary conditions, and experimental trials. Both simulations were given the same values for material properties in the experimental set up, included in Appendix A.

In the CFD simulation constructed by graduate student David Hernandez of the experimental set up (Fig. 8), natural convection along the sides and face was modeled with air as an ideal gas. The bottom of the cold plate was treated as adiabatic. Uniform flow velocity and temperature profiles were also assumed. This numerical simulation is expected to be more accurate than the adiabatic theoretical estimate. Inlet temperature, heat flow into the system, and flow rate were given to predict temperature at points (b) through (g) of the experimental rig shown in Fig. 5. Nine total trials were run with heat flow of 150W, 200W, and 260W; flow rate of 1.4, 2.34, and 3.26 L/min; and inlet temperature of 15°C. The results

Simcenter STAR-CCM+

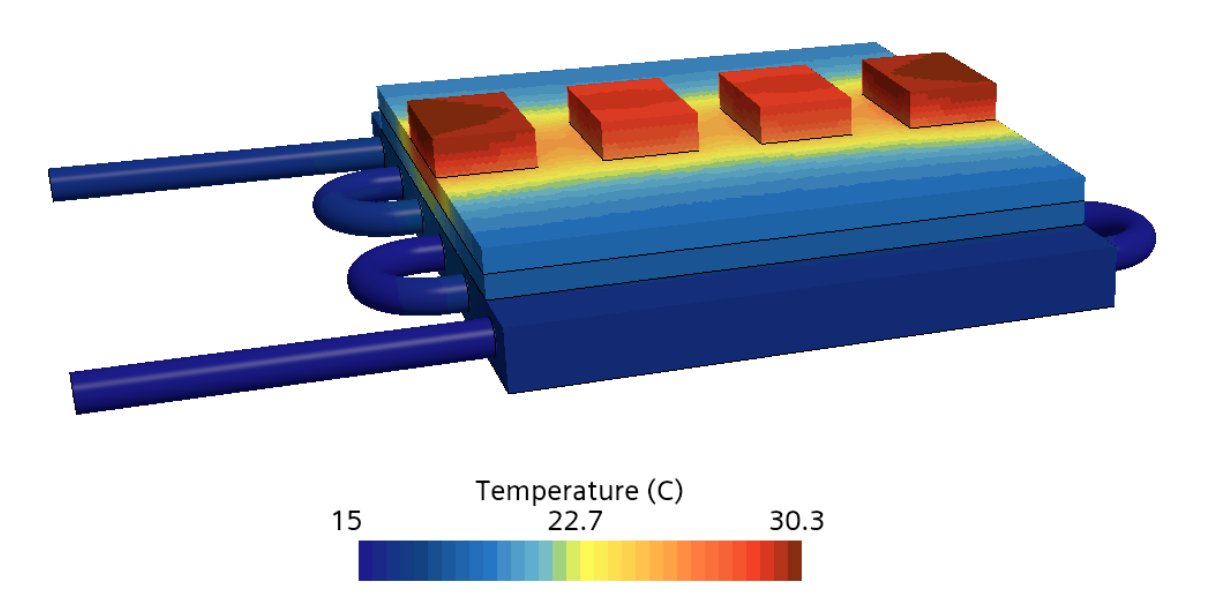


Figure 8: CFD simulation courtesy of David Hernandez with a heat flow in of 200W, inlet temperature of 15° C, and flow rate of 2.34 L/min. This image is from one of nine runs compared to experimental data and PINNs simulation results. The results from all nine CFD runs are given in Appendix B.

from these trials are included in Appendix B.

Postdoctoral Researcher Aniruddha Bora constructed a two-dimensional slice of the test system in python and simulated with PINNs using TensorFlow. The top and bottom surfaces were assumed to be adiabatic, and Robin boundary conditions were prescribed for the edge surfaces. Temperature was also prescribed for the water at each location in the two-dimensional slice as flow was not simulated. Using the convective heat transfer coefficient between the cold plate and the water predicted from the simulation, water flow rate was calculated to compare with experimental results. Similar to the CFD model, temperature at points (a) through (h) of the experimental rig shown in Fig. 5 were predicted. In a manuscript currently under preparation, Dr. Bora further explains the PINNs formulation and explores other assumptions including different boundary conditions [28].

4 Results and Discussion

4.1 Repeatability of Experiment

Establishing repeatability across trials is critical for validation of the experimental set up. Shifting ambient conditions as well as sensor error leads to variation across trials but the variation was not found to be significant.

It is assumed that each ten minute trial is taken at steady state, meaning temperature is expected to be constant and independent of time across trials. In Fig. 9, the temperature readings for each sensor are plotted against time for a trial with experimental conditions of $260\mathrm{W}$, $15^{\circ}\mathrm{C}$ inlet temperature, and $2.4\mathrm{~L/min}$ flow rate. Sensor noise is visualized, with the most precise sensors having the smallest noise and the least precise having the largest noise. There are no significant trends in temperature across the ten minute trial, indicating that the steady state assumption is valid.

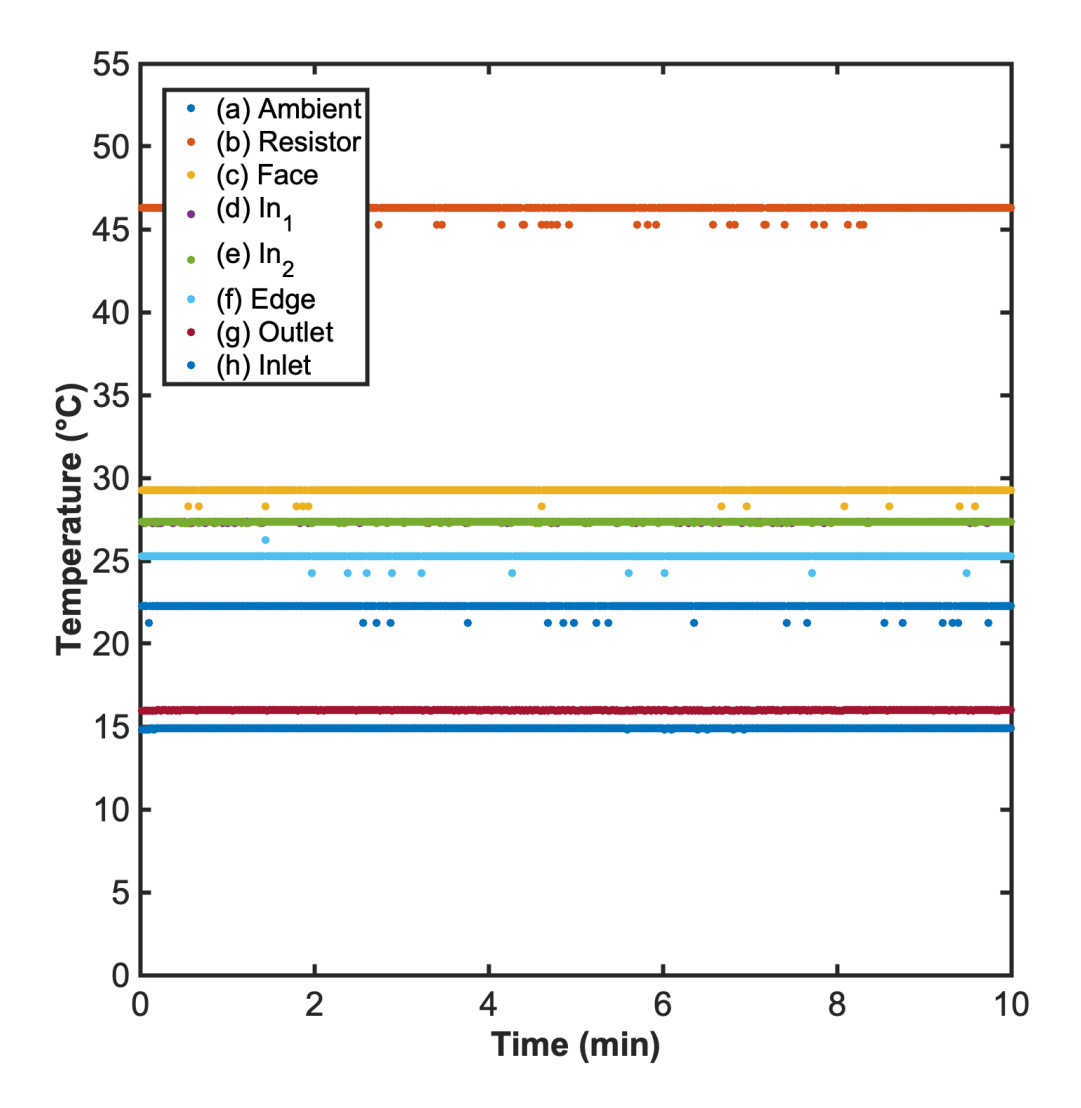


Figure 9: Graph real time sensor readings across a ten minute trial with the experimental conditions of 260W, 15°C inlet temperature, and 2.4 L/min flow rate. As stated in Table 2, the K-type thermocouples have the largest error which is visible in the sensor noise of those four probes: ambient, resistor, face, and side. Discrete steps in temperature are observed due to behavior of the K-type thermocouple amplifier [25].

To determine experimental repeatability, experiments at the edge cases of highest and lowest power were conducted at each different flow rates three times. These trials were taken in a randomized order over several days. For each trial, the steady state temperature averaged across ten minutes at four points is plotted against inlet velocity in Fig 10. Figure 10a shows trials with a heat flow in of 150W and Fig. 10b shows trials with a heat flow in of 260W. As expected, the inlet temperature remains near-constant at 15°C while the rest of the system cools down as flow rate increases. Higher temperatures are observed for a heat flow in of 260W. Trials generally show low variation except on face temperature, which was measured with the K-type thermocouple. As stated in Table 2, the K-type thermocouple has the highest uncertainty out of the three temperature sensors used, which accounts for much for the observed variation. There are no other trends in variation, and the experimental results were found to be repeatable across different days and conditions. Due to low variation between repeated trials, data points for each trial are not always visibly distinguishable in Fig 10.

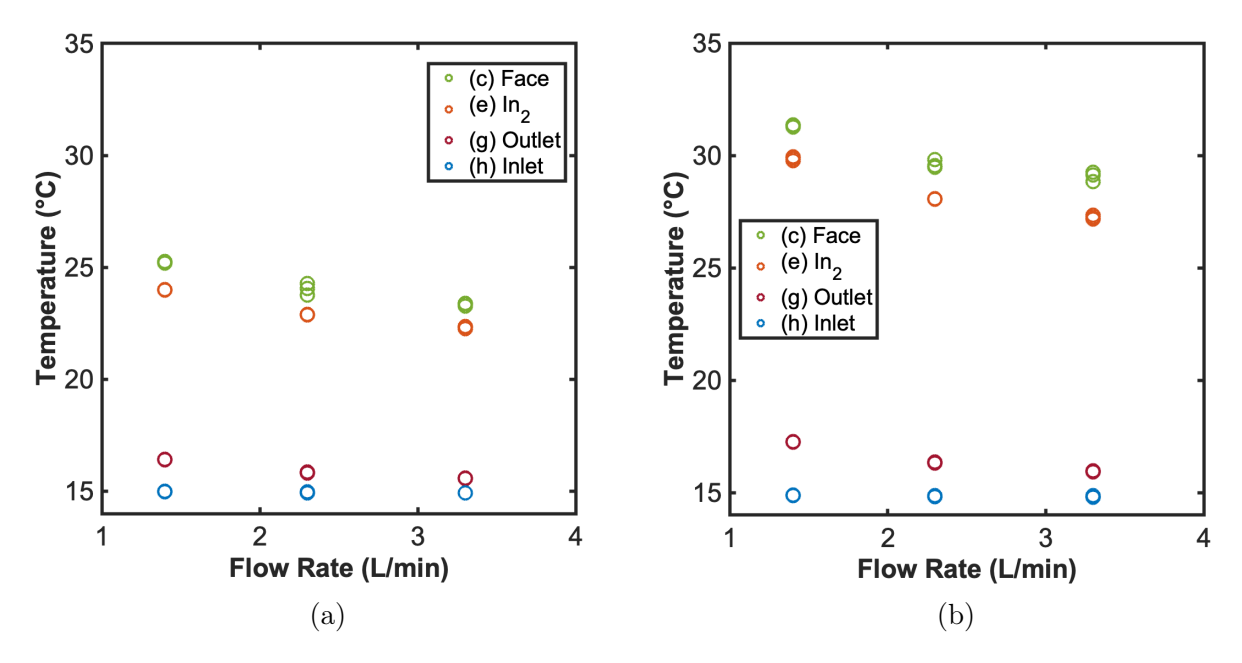


Figure 10: Graphs comparing measured system temperatures for three repeated trials at (a) heat flow Q_{in} of 150W; (b) heat flow Q_{in} of 260W. The inlet temperature is prescribed at 15°C, and is consistent across all nine trials. The other three temperatures are observed to decrease with slower liquid cooling flow rate and lower power across all trials. The highest variation in trials is observed on the face, which is measured with the high-uncertainty K-type thermocouple. As the other three locations have significantly less difference between trials and were measured with more accurate temperature sensors, the thermocouple sensor error largely accounts for observed face temperature variation. Plotted data points for repeated trials with lower variation are visibly near-indistinguishable.

Aside from sensor noise, experimental error is also introduced through variation of ambient conditions, error in the power supplies, and potential non-linear behavior in the fluid system. There is also uncertainty around the material properties of PGS from variability in

the pressure of the experimental rig since thermal conductivity of PGS is pressure dependent.

4.2 Analysis of PINNs With and Without Experimental Data

One major advantage of PINNs is the ability to give the simulation constraints from experimental data for faster convergence and more accurate results. The PINNs simulations were run with the given experimental conditions and the heat equation. The simulations were then run again but with the inclusion of experimental temperature data for the edge and the face of the stack. Figure 11 shows how the PINNs models improve when given experimental data with (a) more accurate flow rate and (b) temperature predictions, and also smaller uncertainty. This is true across a variety of experimental conditions.

CFD is the current standard for thermal-fluid simulation. Comparing the generated temperature profiles on the cross section of the stack in Fig. 12 indicates that PINNs, despite being trained with experimental data, may yield results that deivate from physical expectations. In fact, the PINNs simulation trained on experimental data produced a temperature distribution less similar to CFD than the PINNs simulation without training data. A possible factor contributing to this deviation was setting the thermal resistance of each stack layer as constant even though there is uncertainty in those thermal properties. The temperatures on the edge and face predicted by PINNs were closer to the experimental results than the CFD prediction. However, the asymmetric profile and large temperature difference between the water and cold plate are inconsistent with CFD and theory. CFD also consistently predicted temperature differences between points on the body more accurately, confirming that the CFD simulation profile reflects the experimental set.

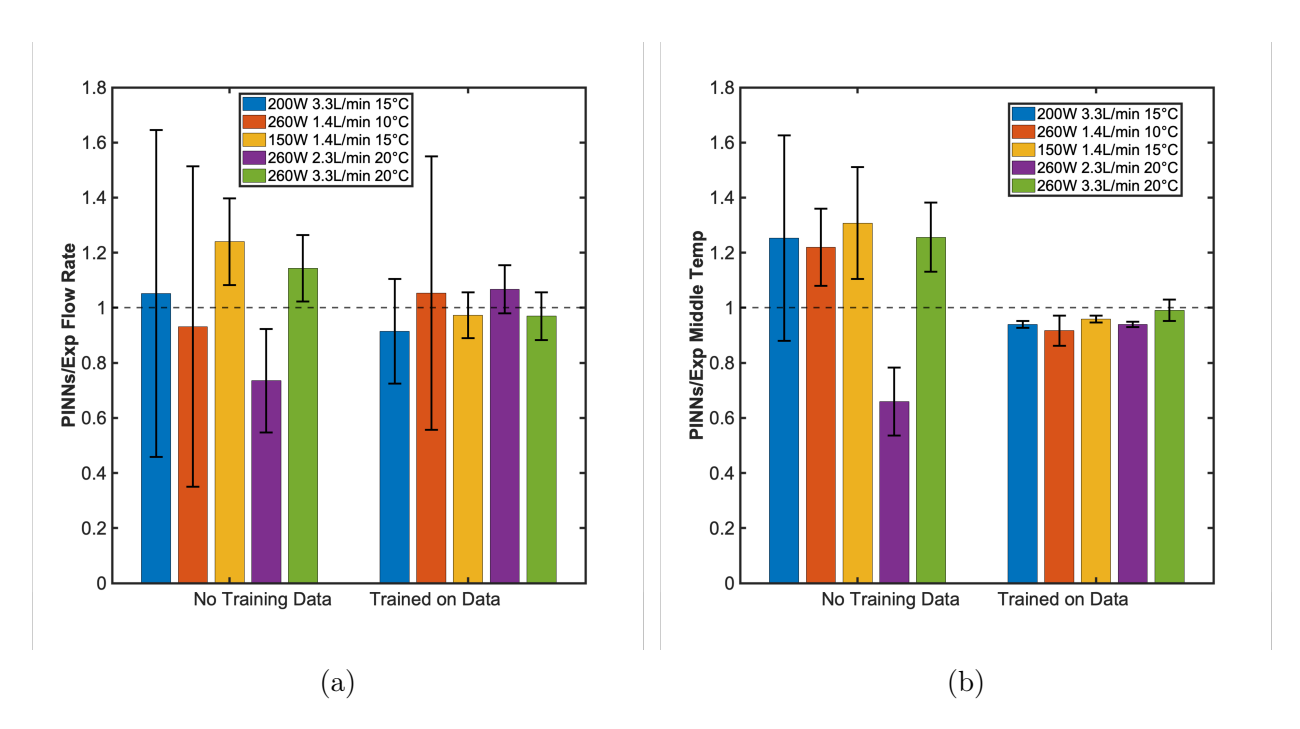


Figure 11: Graphs comparing the predicted values by PINNs, normalized by experimental values for (a) flow rate; (b) middle stack temperature. Error bars represent 95% confidence intervals, calculated with error propagation for experimental and simulation results. The expected flow rate is included in all PINNs simulations trained on experimental data but only included in two for simulations not trained on data. One trial included the expected middle stack temperature for both models with and without training data, but accuracy increased for the simulations given data.

Simcenter STAR-CCM+

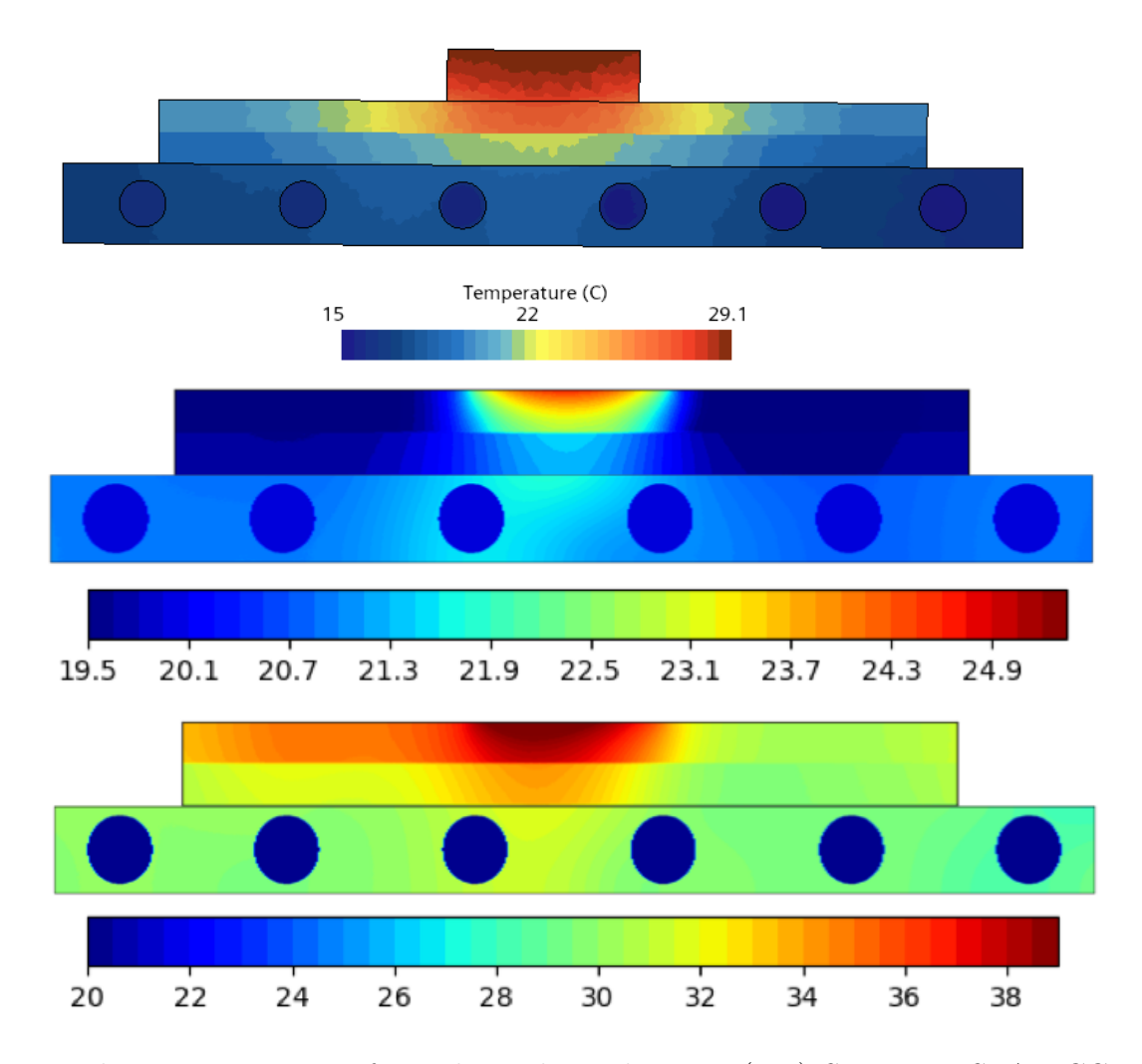


Figure 12: Three cross sections from thermal simulations: (top) Simcenter STAR-CCM+CFD for 200W 15°C 2.34 L/min, courtesy of David Hernandez; (middle) PINNs without data for 260W 20°C 2.34 L/min; (bottom) PINNs with experimental data for 260W 20°C 2.34 L/min. Though the absolute temperatures are expected to differ, the distributions are expected to remain similar. The PINNs simulation not given experimental data has a more similar thermal profile to CFD than the PINNs simulation trained on experimental data. Note the differing colormap scales of the three temperature distributions.

4.3 Comparison of Experimental Results and PINNs to CFD

Experimental results, PINNs, and CFD are generally in agreement, as seen in Fig. 13. Nine different CFD simulations were ran by David Hernandez. Flow rate, inlet temperature, and heat flow in were prescribed for each run, and the simulation predicted temperatures at points (b) through (g) labeled in Fig. 5. Due to inherent randomness in the PINNs simulation, each experimental conditions was run three times then averaged. The PINNs were constrained to the experimentally measured outlet temperature, and used to predicted flow rate and temperature at points (c) through (f) in Fig. 5. Q_{out} is therefore compared across all three data sets as it encompasses the predictions made by both simulations.

All three simulations had results close to the adiabatic case of $Q_{out} = Q_{in}$, with CFD and experimental results staying slightly below as expected. Q_{out} is expected to be slightly less than Q_{in} due to heat flow from the experimental system into the environment, not accounted for in Q_{out} . Larger variations of Q_{out} were observed in PINNs simulation because it is based on optimization and will sometimes settle at locally but not globally optimized solution.

CFD predicted the temperature drop from the face to the middle of the stack more accurately, shown in Fig. 14a. However, Fig. 14b shows that none of the three data sets followed the same trend for the temperature drop across different flow rates.

Figure 15 presents a bar graph of experimental measurements alongside the predictions generated by CFD and PINNs for temperature at four points on the experimental stack: (d) In_1 , (e) In_2 , (f) Edge, and (c) Face. The trials were recorded at 15°C inlet temperature, 150 W, and 1.4 L/min flow rate. The location of the four points are shown in Fig. 5. The PINNs model was trained on experimental edge and face temperatures and matched experimental results for those two points within a 95% confidence interval. Conversely, the CFD model exhibits a discrepancy from the experimental setup across all four points. This outcome is partially due to uncertainties surrounding the thermal resistances of the materials within the experimental rig.

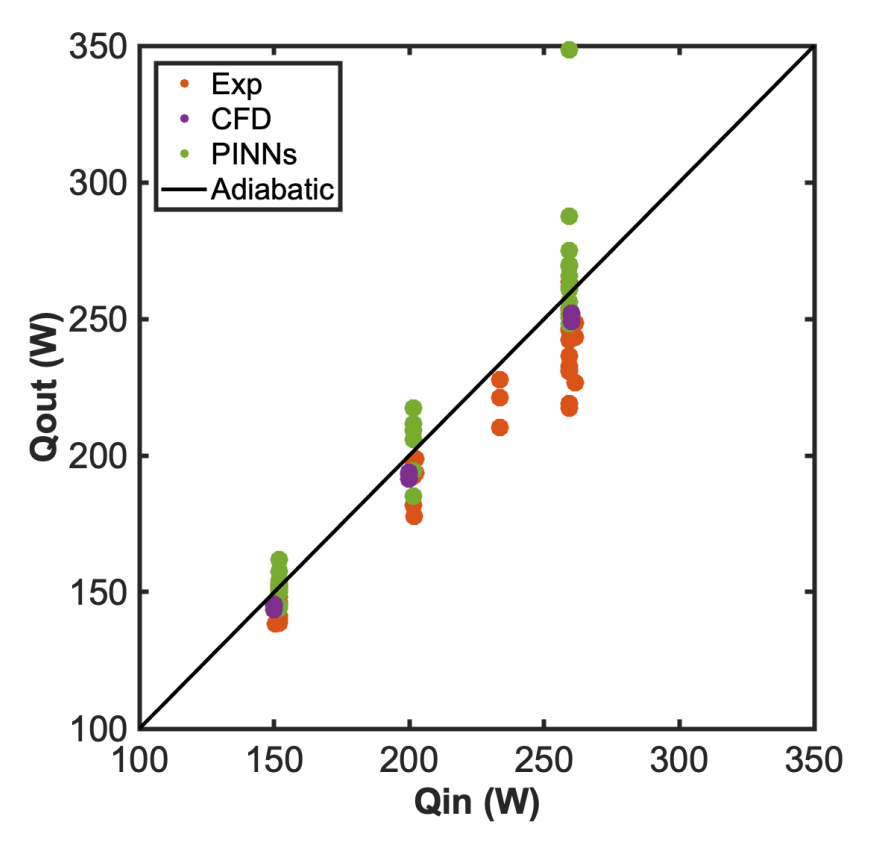


Figure 13: Graph of calculated heat flow out against measured heat flow into the system for experimental results, CFD, and PINNs. A line is drawn for $Q_{out} = Q_{in}$, the adiabatic condition. All three data sets follow the theory as expected, but larger variation is seen in the PINNs data. A significant outlier is seen in the PINNs simulation, which is inherently a stochastic process and will sometimes settle on a non-optimal solution, highlighting the necessity of multiple trials.

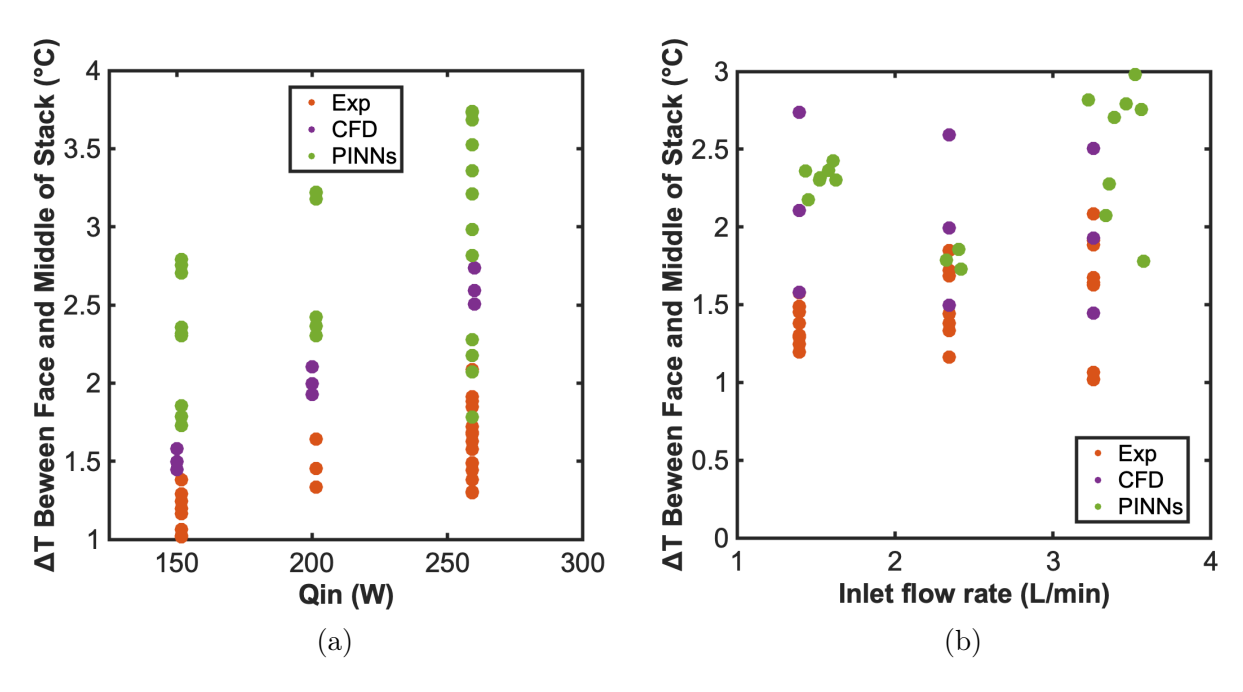


Figure 14: Comparison of the temperature drop across the face and middle of the stack: (a) by heat flow rate; (b) by inlet velocity. Experimental results, CFD, and PINNs simulations all follow a similar upward trend by heat flow rate, but not for inlet velocity. Discrepancies between experimental and simulated results is partially due to sensor error and uncertainty in material thermal properties. Specifically, PGS thermal conductivity is pressure dependent and was only recently characterized at lower pressures [10].

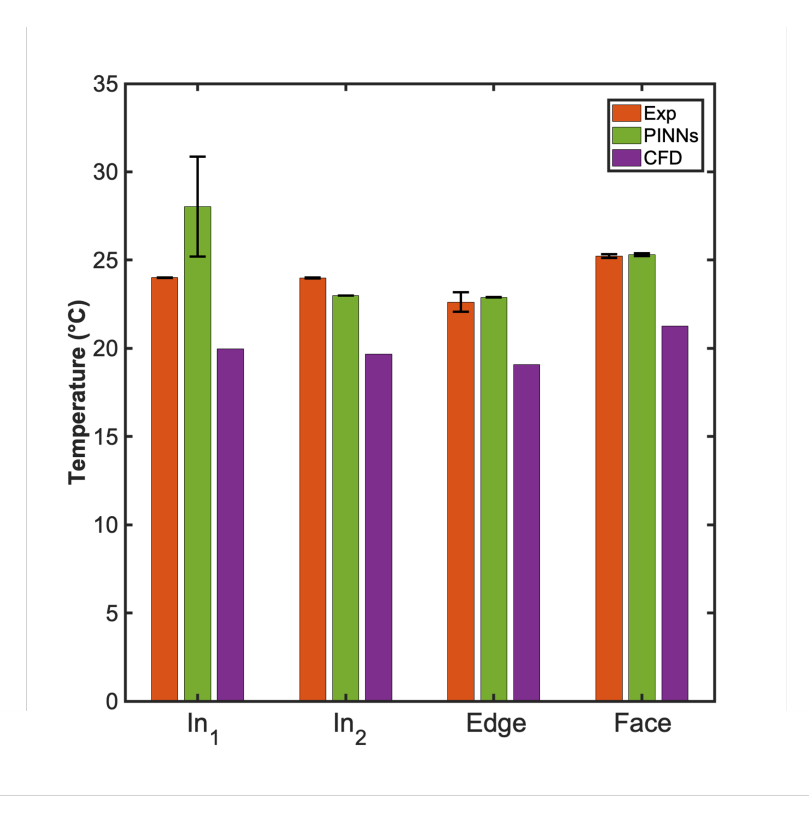


Figure 15: Bar graph showing the experimental measurement as well as CFD and PINNs predictions for temperature at four points on the stack: (d) In_1 , (e) In_2 , (f) Edge, and (c) Face, as labeled in Fig. 5. The experimental conditions were 15°C inlet temperature, 150 W, and 1.4 L/min flow rate. The PINNs model was trained on the experimental edge and face temperature, so it is expected that the experimental value is included in the 95% confidence interval for PINNs. In three cases, the PINNs model predicted values closer to the experimental set up than the CFD model. This is not surprising as the thermal resistance of each material in the experimental rig is not known precisely, though both models were given the same initial estimates.

5 Conclusions and Future Work

While effective solutions to power electronic cooling have been developed, the design constraints around cooling an iPEBB require a new approach. Previous research proposed using dry-interface liquid cooling with pressurized PGS as the thermal interface to meet these design constraints [10]. As the iPEBB continues evolving, rapid thermal simulation accelerates the design and testing process. Experimental data of an analogous physical model to the iPEBB was collected in this thesis under a variety of conditions. The data served to validate CFD as well as train and test new PINNs simulations.

The simulation utilizing PINNs and training data generated temperatures at designated points which aligned closely with experimental results. However, the high accuracy of those specific locations came at the cost of an unrealistic temperature distribution across the entire body, leading to lower accuracy at non-prescribed locations. The PINNs were also subject to outliers and were most accurate when averaged over several trials, with the standard deviation across trials decreasing when trained on experimental data. CFD produced precise results with temperature drops matching experimental results more closely, both across the inlet and outlet and from the face to middle of the stack. Still, the absolute temperatures predicted by CFD do not match experimental results exactly. The discrepancies in both PINNs and CFD may be partially accounted for by uncertainty in material thermal properties of the stack. The CFD model also produced a more realistic temperature distribution, which is expected as fluid flowing through the system was included in the simulation. The PINNs model prescribed the fluid temperature and solely simulated heat flow. While both the PINNs and CFD models exhibit strengths and limitations in predicting temperature distributions within the system, the discrepancies between simulated and experimental results underscores the necessity for experiment data sets. The collected experimental data set in this thesis is publicly available for the training and testing of computational models.

Ongoing research aims to improve the agreement between the simulated and observed temperature profiles in PINNs. Developments include experimenting with various boundary conditions and modifying the neural network architectures. This additional research will be discussed in the future manuscript of Bora *et al.* [28].

Future work would also include research using DeepONet/Operator-based networks, enabling generalization across parameters and conditions. Constructing a DeepONet would also allow faster simulations for rapid evaluation of iPEBB cooling designs. Neural networks are becoming a powerful simulation tool, and the evaluation approach employed in this thesis is applicable to a broad range of complex systems.

References

- [1] "2018 Initial IMO Strategy," International Maritime Organization. (Jul. 2018), URL: https://www.imo.org/en/OurWork/Environment/Pages/Vision-and-level-of-ambition-of-the-Initial-IMO-Strategy.aspx (visited on 05/10/2024).
- [2] "IMO's Work to Cut GHG Emissions from Ships," International Maritime Organization. (Jul. 2023), URL: https://www.imo.org/en/MediaCentre/HotTopics/Pages/Cutting-GHG-emissions.aspx (visited on 05/10/2024).
- [3] U. S. Navy, "Naval power and energy systems technology development roadmap," Naval Sea Systems Command, Washington Navy Yard, DC, 2019 NPES TDR, 2019. URL: https://www.navsea.navy.mil/Portals/103/Documents/2019_NPES_TDR_Distribution_A_Approved_Final.pdf?ver=2019-06-26-132556-223 (visited on 05/10/2014).
- [4] J. Kersey, N. D. Popovich, and A. A. Phadke, "Rapid battery cost declines accelerate the prospects of all-electric interregional container shipping," *Nature Energy*, vol. 7, no. 7, pp. 664–674, Jul. 1, 2022, ISSN: 2058-7546. DOI: 10.1038/s41560-022-01065-y. URL: https://doi.org/10.1038/s41560-022-01065-y.
- [5] S. Guo, Y. Wang, L. Dai, and H. Hu, "All-electric ship operations and management: Overview and future research directions," eTransportation, vol. 17, p. 100251, 2023, ISSN: 2590-1168. DOI: https://doi.org/10.1016/j.etran.2023.100251. URL: https://www.sciencedirect.com/science/article/pii/S2590116823000267.
- [6] L. Peterson *et al.*, "Power electronic power distribution systems (PEPDS)," Electric Ship Research and Design Consortium, DCN # 43-9043-22, 2022.
- [7] J. C. Ordonez, C. Sailabada, J. Chalfant, et al., "Thermal management for ship electrification approaches for power electronic building blocks and power corridors," *IEEE Transactions on Transportation Electrification*, pp. 1–1, 2024. DOI: 10.1109/TTE.2024. 3391209.
- [8] N. Rajagopal, C. DiMarino, R. Burgos, I. Cvetkovic, and M. Shawky, "Design of a high-density integrated power electronics building block (iPEBB) based on 1.7 kV SiC MOSFETs on a common substrate," in 2021 IEEE Applied Power Electronics Conference and Exposition (APEC), 2021, pp. 1–8. DOI: 10.1109/APEC42165.2021. 9487167.
- [9] D. E. Hernandez, "Thermal analysis of indirect liquid cooling for the Navy integrated power electronics building block," Undergraduate thesis, Massachusetts Institute of Technology, Cambridge, MA, 2023.

- [10] J. G. Padilla, "Characterizing the thermal behavior of pyrolytic graphite sheets (PGS) at low interface pressures," Master's thesis, Massachusetts Institute of Technology, Cambridge, MA, 2023.
- [11] M. Raissi, P. Perdikaris, and G. Karniadakis, "Physics-informed neural networks: A deep learning framework for solving forward and inverse problems involving nonlinear partial differential equations," Journal of Computational Physics, vol. 378, pp. 686–707, 2019, ISSN: 0021-9991. DOI: https://doi.org/10.1016/j.jcp.2018.10.045. URL: https://www.sciencedirect.com/science/article/pii/S0021999118307125.
- [12] C. J. Sarao, "Design and modeling of pneumatic mechanism for improved indirect liquid cooling of shipboard power electronics," M.S. thesis, Massachusetts Institute of Technology, Cambridge, MA, 2024.
- [13] Y. Cheng, G. Xu, D. Zhu, W. Zhu, and L. Luo, "Thermal analysis for indirect liquid cooled multichip module using computational fluid dynamic simulation and response surface methodology," *IEEE Transactions on Components and Packaging Technologies*, vol. 29, no. 1, pp. 39–46, 2006. DOI: 10.1109/TCAPT.2005.848589.
- [14] Z. Liu, Y. Xu, H. Wu, P. Wang, and Y. Li, "Data-driven control co-design for indirect liquid cooling plate with microchannels for battery thermal management," International Design Engineering Technical Conferences and Computers and Information in Engineering Conference, vol. 3A: 49th Design Automation Conference (DAC), V03AT03A048, Aug. 2023. DOI: 10.1115/DETC2023-116921. eprint: https://asmedigitalcollection.asme.org/IDETC-CIE/proceedings-pdf/IDETC-CIE2023/87301/V03AT03A048/7061091/v03at03a048-detc2023-116921.pdf. URL: https://doi.org/10.1115/DETC2023-116921.
- [15] L. McClenny and U. Braga-Neto, Self-adaptive physics-informed neural networks using a soft attention mechanism, 2022. arXiv: 2009.04544 [cs.LG].
- [16] S. J. Anagnostopoulos, J. D. Toscano, N. Stergiopulos, and G. E. Karniadakis, "Residual-based attention in physics-informed neural networks," *Computer Methods in Applied Mechanics and Engineering*, vol. 421, p. 116 805, 2024, ISSN: 0045-7825. DOI: https://doi.org/10.1016/j.cma.2024.116805.
- [17] J. Yu, L. Lu, X. Meng, and G. E. Karniadakis, "Gradient-enhanced physics-informed neural networks for forward and inverse PDE problems," *Computer Methods in Applied Mechanics and Engineering*, vol. 393, p. 114823, 2022, ISSN: 0045-7825. DOI: https://doi.org/10.1016/j.cma.2022.114823.
- [18] G. Zhang, H. Yang, Y. Chen, and X. Zheng, DASA-PINNs: Differentiable adversarial self-adaptive pointwise weighting scheme for physics-informed neural networks. DOI: http://dx.doi.org/10.2139/ssrn.4376049.
- [19] L. Lu, P. Jin, G. Pang, Z. Zhang, and G. E. Karniadakis, "Learning nonlinear operators via DeepONet based on the universal approximation theorem of operators," *Nature Machine Intelligence*, vol. 3, no. 3, pp. 218–229, Mar. 1, 2021, ISSN: 2522-5839. DOI: 10.1038/s42256-021-00302-5. URL: https://doi.org/10.1038/s42256-021-00302-5.

- [20] S. Goswami, A. Bora, Y. Yu, and G. Karniadakis, "Physics-informed deep neural operator networks," in *Machine Learning in Modeling and Simulation: Methods and Applications*, T. Rabczuk and K.-J. Bathe, Eds., Springer, Cham, Apr. 2023, pp. 219–254. DOI: https://doi.org/10.1007/978-3-031-36644-4.
- [21] S. Cai, Z. Wang, C. Chryssostomidis, and G. E. Karniadakis, "Heat transfer prediction with unknown thermal boundary conditions using physics-informed neural networks," Fluids Engineering Division Summer Meeting, vol. 3: Computational Fluid Dynamics; Micro and Nano Fluid Dynamics, V003T05A054, Jul. 2020. DOI: 10.1115/FEDSM2020-20159. URL: https://doi.org/10.1115/FEDSM2020-20159.
- [22] S. Cai, Z. Wang, S. Wang, P. Perdikaris, and G. E. Karniadakis, "Physics-Informed Neural Networks for Heat Transfer Problems," Journal of Heat Transfer, vol. 143, no. 6, p. 060 801, Apr. 2021, ISSN: 0022-1481. DOI: 10.1115/1.4050542. eprint: https://asmedigitalcollection.asme.org/heattransfer/article-pdf/143/6/060801/6688635/ht\
 _143_06_060801.pdf. URL: https://doi.org/10.1115/1.4050542.
- [23] $I\text{-}Scan^{TM}$ and High Speed $I\text{-}Scan^{TM}$ User Manual, Tekscan, Inc., South Boston, MA, 2018.
- [24] "G1/2" water flow hall sensor switch flow meter 1-30L/min," Digiten. (2024), URL: https://www.digiten.shop/products/digiten-g1-2-water-flow-hall-sensor-switch-flow-meter-1-30l-min (visited on 05/10/2024).
- [25] Precision thermocouple amplifiers with cold junction compensation, AD8495, Rev. D, Analog Devices, 2018.
- [26] "Surface temperature sensor," Vernier Science Education. (2024), URL: https://www.vernier.com/product/surface-temperature-sensor (visited on 05/10/2024).
- [27] "Temperature sensor waterproof (DS18B20)," SparkFun Electronics. (2024), URL: https://www.sparkfun.com/products/11050 (visited on 05/10/2024).
- [28] A. Bora, I. Alvarez, J. Chalfant, C. Chryssostomidis, and G. E. Karniadakis, "PINNs formulation for estimating coolant velocity and temperature for effective heat sink for PEBBs."
- [29] "Aluminum 6061-T6 (UNS AA96061)," National Institute of Standards and Technology. (Jun. 2021), URL: https://www.nist.gov/mml/acmd/aluminum-6061-t6-uns-aa96061 (visited on 05/10/2024).
- [30] "Material property data," MatWeb, LLC. (2024), URL: https://www.matweb.com (visited on 05/10/2024).

Appendix A

Material Properties

The total effective resistance is approximately as the sum of the conductive resistances across each layer, which are shown in Table 3.

Table 3: Geometry and Properties of Materials in the Experimental Rig

Material	Thermal Conductivity (W/mK)	Dimensions (mm)
6061-T6 Al	152 [29]	$152.4 \times 152.4 \times 6.35$
PGS (4.2 psi)	0.842 [10]	$152.4 \times 152.4 \times 0.2$
MIC 6 Al	142 [30]	$152.4 \times 152.4 \times 6.35$
304 SS	16.2 [30]	OD 9.525, ID 8.105

Appendix B

CFD Simulation Results

Simulation results, courtesy of MIT graduate student David Hernandez, are listed in Table 4. All temperatures at locations (c) through (h) are in $^{\circ}$ C. Sensor locations are labeled in Fig. 5. Inlet temperature, flow rate, and Q_{in} were prescribed.

Table 4: CFD Simulation Results

Q_{in} (W)	Flow rate (kg/s)	(c) Face	(d) In ₁	(e) In ₂	(f) Edge	(h) Inlet	(g) Outlet
150	0.0234	21.258	19.972	19.680	19.078	15	16.487
150	0.0391	20.186	18.887	18.690	18.006	15	15.886
150	0.0545	19.794	18.488	18.348	17.611	15	15.631
200	0.0234	23.343	21.629	21.239	20.436	15	16.982
200	0.0391	21.915	20.182	19.921	19.008	15	16.181
200	0.0545	21.392	19.651	19.464	18.481	15	15.841
260	0.0234	25.846	23.617	23.110	22.067	15	17.576
260	0.0391	23.989	21.737	21.397	20.211	15	16.536
260	0.0545	23.309	21.046	20.803	19.525	15	16.093